OPTICAL MEMS SENSORS FOR INSTANTANEOUS WALL-SHEAR STRESS MEASUREMENTS IN TURBULENT BOUNDARY-LAYER FLOWS

Nima Ebrahimzade
School of Engineering
Newcastle University
Newcastle upon Tyne, NE1 7RU, UK
Nima.ebrahimzade@ncl.ac.uk

Jose Portoles
School of Engineering
Newcastle University
Newcastle upon Tyne, NE1 7RU, UK

Peter Cumpson
Mark Wainwright Analytical Centre
University of New South Wales
Sydney, New South Wales, NSW 2052, Australia
p.cumpson@unsw.edu.au

Michael Wilkes
School of Engineering
Newcastle University
Newcastle upon Tyne, NE1 7RU, UK
Michael.wilkes@ncl.ac.uk

Richard D. Whalley
School of Engineering
Newcastle University
Newcastle upon Tyne, NE1 7RU, UK
Richard.whalley@ncl.ac.uk

ABSTRACT

Presented is a new technique based on micro-electro-mechanical systems (MEMS) technologies for accurately measuring instantaneous wall-shear stress, τ_w, in turbulent air flows. Utilising this new technique, direct measurement of the instantaneous wall-shear stress is performed by tracking the displacement of a miniature flush-mounted floating element, which is on the order of hundreds of microns squared. In a series of wind tunnel experiments over a Reynolds number range of $Re_\tau = u_\tau \delta / \nu = 600$ to 1320 (where u_τ, δ, and ν are the friction velocity, boundary-layer thickness, and kinematic viscosity, respectively), the instantaneous wall-shear stress is measured within the turbulent boundary-layer flow simultaneously by the MEMS sensors and laser Doppler velocimetry (LDV). Good agreement is observed across these two independent measurement techniques. A micro-spring and optical Moiré fringe pattern transduction are employed to enhance the sensitivity of the sensors by 120 times compared to existing sensors on the market. The developed MEMS wall-shear stress sensors have a sensitivity range of $23-740$ nm/Pa, an accuracy range of $1.4-2.4\%$, and a repeatability range of $0.7-1.9\%$.

INTRODUCTION

Obtaining instantaneous measurement of wall-shear stress in wall-turbulent flows, particularly in air flows, is notoriously difficult and has significant fundamental and industrial importance. Thermal sensors such as hot-film and hot-wire probes can be calibrated to determine the wall-shear stress. For the hot-film probes to work, the thermal conductivity of the fluid, λ, should be larger than the thermal conductivity of the material on the wall (Alfredsson and Johansson 1988). Since this is not the case for air flows ($\lambda = 0.024$ W/mk), the wall-shear stress fluctuations measurement is underestimated, and hence, hot-film probes are normally used for mean wall-shear stress measurement and qualitative measurements in air flows (Whalley, et al. 2019). Hot-wire probes can be used to measure the wall-shear stress by applying the near-wall velocity gradient technique (Hutchins and Choi 2002). Hot-wire probes have a high-frequency response, however, the heat conduction from the probe to the wall influences the sensor's performance. Additionally, as the thickness of the viscous sublayer decreases with an increase in the Reynolds number, it becomes challenging to get an adequate number of points from within the viscous sublayer as the probe gets close to the wall. Hot-film and hot-wire probes are directionally insensitive and hence, cannot be used to detect bi-directional wall-shear stress. LDV can determine the directional wall-shear stress by using the near-wall velocity gradient technique (Örlü and Vinuesa 2020). Direct MEMS sensors measure the displacement of a flush-mounted structure due to the applied wall-shear stress. Various types of devices have been developed using capacitive (Barnard et al. 2016; Chandrasekharan et al. 2011; Mills et al. 2018), piezoresistive (Shajii et al. 1992; Barlian et al. 2007; Li et al. 2008), and optical (Tseng et al. 2003; Horowitz et al. 2004; Chen et al. 2011; Mills et al. 2016) transduction methods. Capacitive and piezoresistive sensors are susceptible to environmental parameters such as temperature, humidity, and Electromagnetic Interference (EMI). Optical transduction benefits from the absence of electronic connections to the sensor die, leading to immunity to environmental parameters.

To date MEMS wall-shear stress sensors, even though they have been in development for more than 20 years, have not seen routine adoption. In this study, we have developed and characterised accurate, low-cost optical MEMS sensors which can accurately measure the instantaneous wall-shear stress in turbulent boundary-layer flows. Additionally, we have developed the underpinning analytical methods that permit the design of sensors for a range of applications.

SENSOR DEVELOPMENT

The MEMS wall-shear stress sensors consist of a floating element with a width and length of W_e and L_e and suspended on each side by specially designed micro-springs with a width and length of W_t and L_t; see figure 1a of an image of a microfabricated MEMS wall-shear stress sensor. As air flows over the MEMS sensor, the floating element is free to move, as a result of the micro-spring arrangements, in the direction

(a)

(b)

(c)
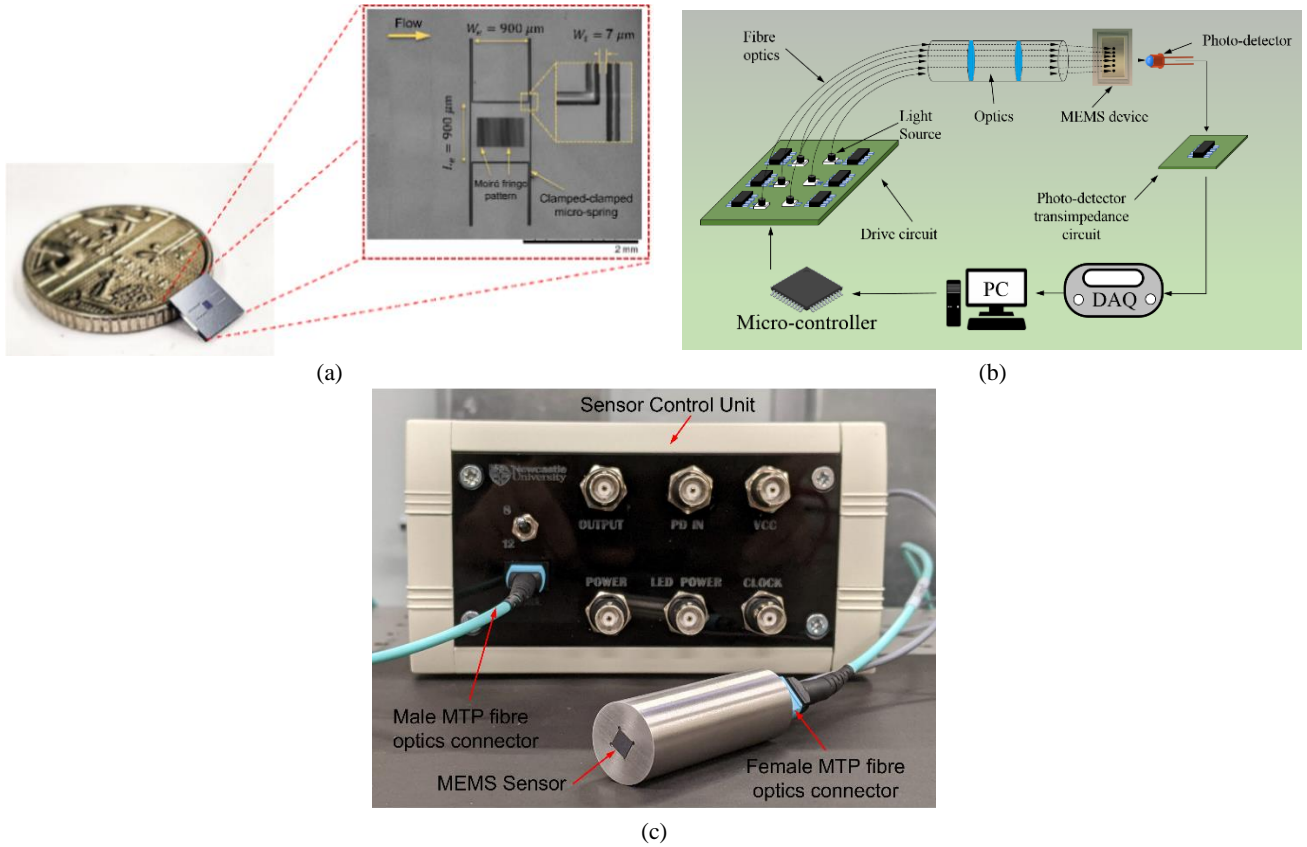
Figure 1. (a) SEM image of a MEMS wall-shear stress sensor on a 5mm×5mm die, (b) Schematics of the rippling optoelectronics for the MEMS wall-shear stress sensors, (c) Image of the sensor packaging and the sensor control unit.

of the fluid flow. The displacement of the devices due to the instantaneous wall-shear stress is as low as tens of nanometers and hence, Moiré fringe transduction (Amidror, 2009) is used to amplify the displacement of the sensors by a factor of 60 to 100 times. Moiré fringe pattern is generated during the microfabrication process by superposition of two sets of finely spaced gold gratings with slightly different spatial pitches, g_1 and g_2. The superposition of these grating sets generates a periodic optical pattern of light and dark regions with a larger spatial period, G. The displacement of the Moiré fringe pattern, Δ, is linearly linked to the mechanical displacement of the floating element, δ_{τ_w}, by $\Delta = (\frac{G}{g_1})\delta_{\tau_w}$, where G/g_1 is the amplification factor. The periodic dark and light pattens on the Moiré fringe pattern can be expressed in terms of the sum of sinusoidal functions, where the amplitude, period, and the initial phase are fixed, due to the microfabrication process, and the movement of the Moiré fringe pattern only results in a phase shift (Chen et al, 2011). In the presented MEMS wall-shear stress sensors, one of the gold gratings set is fixed on a transparent substrate, whilst the second set is free to move with the sensor's floating element, which results in the movement of the Moiré fringe pattern. To detect the motion of the Moiré fringe pattern, a light spot is rapidly scanned across the Moiré fringe pattern. As shown in figure 1b, rippling optoelectronics consists of an array of twelve Light Emitting Diodes (LEDs), an array of twelve fibre optic cables, a pair of aspheric lenses and a single photodiode is used to track the displacement of the Moiré fringe pattern. The light from each LED is launched down a dedicated fiber optic cable and is then focused via a pair of lenses to a small spot of light, typically 10's of microns in diameter, on the backside of the Moiré fringe pattern. The light spot is then reflected from the Moiré

fringe pattern into the photodiode. The light spots are rippled in sequence at a frequency higher than any in the flow to extract the sinusoidal response of the Moiré fringe pattern. As the MEMS sensor oscillates due to the applied wall-shear stress, the phase of the sinusoidal response of the Moiré fringe pattern is tracked with time utilizing the fast-scanning optoelectronics, which is calibrated to measure the instantaneous wall-shear stress. Inspection of the microfabricated devices using Scanning Electron Microscopy (SEM) demonstrated that the geometrical parameters of the devices were in excellent agreement with the design parameters; see figure 1a. Additionally, the formation of the Moiré fringe pattern on the MEMS wall-shear stress sensors can be observed with the distinguishable dark and light bands.

Experimental Setup

Static calibration of the packaged MEMS wall-shear stress sensors (figure 1c) was carried out in a laminar flow rig with a cross-section dimensions of 0.5×80 mm and a length of 2 m, in which the mean wall-shear stress was determined via the pressure gradient, $\partial \overline{P}/\partial x$, measurement as $\tau_w = -h\partial \overline{P}/\partial x$, where h is the channel half height. A 30 mm diameter plugging port was located 1.65 m down the flow inlet, allowing for the MEMS wall-shear stress sensors to be mounted directly into the channel base. The pressure gradient measurement was performed over a 200 mm distance with the positive and negative ports being on the upstream and downstream of the MEMS sensors, respectively; see figure 2a. The inlet compressed air flow rate was controlled by adjusting a needle valve, where the flow rate was measured using a Dawyer RMA-8-BV flowmeter, with an accuracy of ±4%.

Table 1. Specifications of selected MEMS wall-shear stress sensors.

Device	W_e (μm)	L_e (μm)	W_t (μm)	L_t (μm)	Sensitivity (nm/Pa)	Accuracy	Repeatability	f_0 (kHz)
MEMS 1	1000	1000	7	1500	730	2.1%	0.68%	1.016
MEMS 2	800	800	7	900	120	1.5%	0.9%	2.835
MEMS 3	1000	1000	10	800	42	1.41%	1.1%	4.346
MEMS 4	800	500	500	12	38	1.8%	1.24%	8.37
MEMS 5	650	500	500	10	56	1.76%	0.86%	7.38
MEMS 6	650	500	500	10	53	2.36%	1.96%	7.38

The pressure difference across the calibration rig and on two sides of the sensors was measured using a Betz PARW 79 manometer with an accuracy of ± 50 μm H_2O and a dynamic range of 0-400 mmH_2O. A Voltcraft PL-125-T2USBVS thermometer with an accuracy of $\pm 0.15\%$ was implemented at the flow outlet to record the air flow temperature during the calibration.

Dynamic characterisation of the sensors was performed under a Zygo NewView 5000 profilometer by using the Dynamic Metrology Module (DMM) and a stroboscopic light source, as illustrated in figure 2b. The devices were mounted at the 5mm×5mm top surface of a Thorlabs PN5FC2 low voltage shear piezoelectric stack and they were actuated by a drive signal from a Pragmatic 2416A Arbitrary Waveform Generator (AWG).

(a)

(b)   (c)
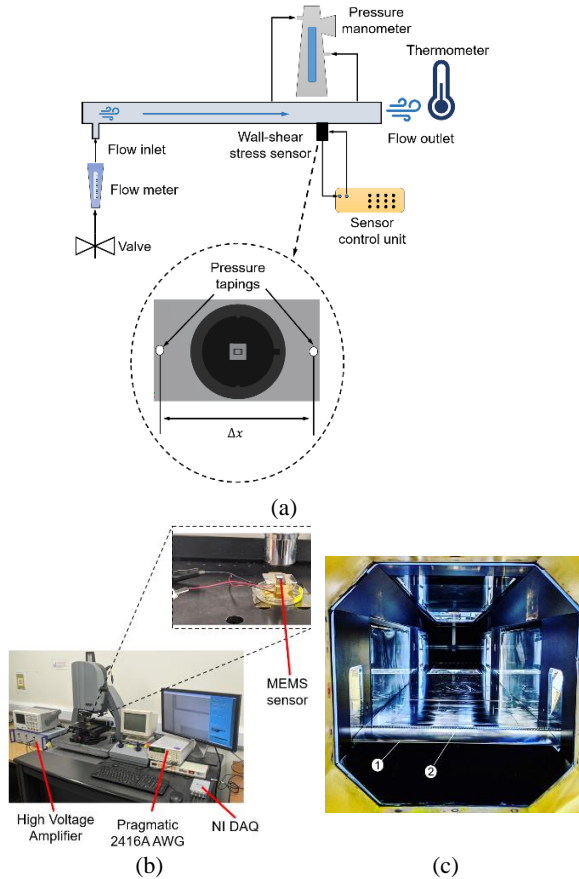
Figure 2. (a) Schematics of the MEMS sensors calibration setup; (b) experimental setup for the dynamic characterisation. The MEMS sensors were mounted on the top surface of a 2D piezoelectric shear stack; (c) an image of the wind tunnel test section, showing (1) the elliptical leading edge and (2) the turbulent trip.

Turbulent boundary-layer measurements were conducted 1.8 m ($x^+ = x\,u_\tau/\nu = 28068$ to 68064) downstream of a 3 m long flat plate inside an open-loop wind tunnel with an inner geometry of 350mm×460mm ($h \times w$). The boundary-layer was developed on a flat plate, manufactured from a 20mm thick Formica. The flow was tripped into the turbulent boundary-layer by using a zig-zag shape trip (Elsinga and Westerweel, 2012) that was attached to a super elliptic leading edge as shown in figure 2c. The turbulent trip was manufactured from a 3mm acrylic, and laser-cut into a zig-zag shape with a pitch of 6mm, which is 11mm in width and extended across the width of the flat plate. A flap was adjusted at the test section trailing edge to a maximum angle of $47.6°$ in $3.4°$ increments to alter the stagnation point of the flow at the tip of the leading edge, resulting in a zero-pressure gradient flow along the test section.

A TSI LDV system, consisting of two 1W STM/SLM Genesis MX series continuous-wave lasers with a wavelength of 514 nm and 488 nm, was utilised for the turbulent boundary-layer measurement alongside the MEMS sensors. A TSI RV4480 optical lens beam expander was used to focus the laser beams into the test section, generating a measurement volume with a diameter of 50 μm ($d^+ = d\,u_\tau/\nu = 0.78$ to 1.9) and a length of 250 μm ($l^+ = d\,u_\tau/\nu = 3.96$ to 9.49). A 3-axis Isel traverse system was used to traverse the intersecting laser beams in the wall-normal direction with a resolution of 5 μm. A TSI receiver with a focal length of 300 mm was used in a forward scatter mode to pick up the scattered light and transmit the collected signal into an FSA3500 processor to convert the signal to velocity. A TSI atomizer filled with Di-Ethyl-Hexyl-Sebacat (DEHS), introduces seeding particles of 1 μm diameter into the flow. The data from the MEMS sensors were sampled using a 16-bit National Instrument NI-9215 card.

Experimental Results

Specifications of developed MEMS sensors that were used in this study are presented in Table 1. Here, six different types of MEMS wall-shear stress sensors with different geometries were packaged up and tested.

MEMS wall-shear stress sensors were calibrated over a wall-shear stress range of $\tau_w = 0-5.3$ Pa. The output signals of the MEMS sensors were recorded for a period of 60 seconds at a 10 kHz sampling rate, for each wall-shear stress point. For each device two calibration runs were performed to check for the repeatability of the sensors' reading. Shown in figure 3a is the displacement of the Moiré fringe pattern's sine curve as a result of the phase shift due to the applied wall-shear stress in the calibration rig, captured by the photodiode response. The inset in figure 3a demonstrates the photodiode response from a light spot on a fixed location on the Moiré fringe pattern. Here, it can be seen that a change in the applied wall-shear stress results in a change in the light intensity as a consequence of the Moiré fringe pattern light and dark bands displacement.

Accuracy of the MEMS sensors was obtained using the highest deviation of the measured value with the sensors from the ideal value of the wall-shear stress, which can be calculated from the calibration curve (Fraden, 2004). This deviation is expressed in terms of the difference between the value of the wall-shear stress, which has been traced back from the sensors reading and the actual input value of wall-shear stress. The repeatability error of the MEMS sensors was estimated using the data points from two experimental runs (Fraden, 2004). The calibration results, figure 3b, indicate a mechanical sensitivity range of $23-730$ nm/Pa, an accuracy range of $1.4-2.4\%$, and a repeatability range of $0.7-1.9\%$.

Table 2. Turbulent flow wall-shear stress parameters measured by MEMS sensors and LDV.

	Device	$\overline{\tau_w}$ (Pa)	SD_{τ_w}	S_{τ_w}	K_{τ_w}
$Re_\tau = 910$	LDV	0.124	0.0564	1.1425	5.24
	MEMS 1 (centre)	0.121	0.0457	1.1361	5.14
	MEMS 2 (left)	0.116	0.0421	1.1378	5.13
	MEMS 3 (right)	0.115	0.0408	1.1212	5.02
$Re_\tau = 1320$	LDV	0.399	0.1858	1.1465	5.22
	MEMS 6 (centre)	0.391	0.1552	1.1307	5.16
	MEMS 3 (left)	0.387	0.1544	1.1394	5.18
	MEMS 4 (right)	0.393	0.154	1.1426	5.21

To capture the frequency response of the devices, a quick frequency sweep was performed for the range of 1 Hz up to 10 kHz. When the devices were in their resonant frequency threshold, their images became blurry as the exposure time of the image sensor on the Zygo NewView 5000 was not able to resolve high speed motion of the sensors. To resolve the sensors' motion under the excitation, the frequency difference between the drive signal and the strobe light were set to be equal to one, whilst the phase delay between the two signals were set to zero. This resulted in the visualisation of the sensors' displacement at 1 Hz, which can be resolved by the image sensor. The video of the sensors motion at each frequency was recorded for a period of 10 seconds and then converted into the frames. An image processing algorithm was performed on the individual frames to extract the displacement time response and frequency response of the devices. Dynamic characterisation of the devices indicates a resonant frequency range of $1-8.4$ kHz and a dynamic range of 79-109 dB: see figure 2c.

In a series of wind tunnel experiments over a flow speed range of U_∞ = 6 to 15 m/s (Re_τ = 600 to 1320), the instantaneous wall-shear stress was measured within the turbulent boundary-layer simultaneously by the MEMS sensors and LDV. Prior to the wall-shear stress measurements, canonical turbulent boundary-layer quantification was performed in two spanwise locations, to make sure that the canonical turbulent boundary-layer profiles are similar across the span at a specific streamwise location ($x^+ = x\,u_\tau/\nu = $ 28068 to 68064). This was investigated through the statistical values of the turbulent flow. The first set of the canonical turbulent boundary-layer profiles was measured at the centreline of the test section ($z^+ = zu_\tau/\nu = 0$), where the central MEMS sensor was implemented, whilst the second data set was captured 75mm ($z^+ = 1166$ to 2828) in the spanwise direction and at the location of the MEMS sensor on the right side. Figure 4a shows the time-averaged streamwise velocity profile taken by LDV at $z^+ = 0$, where the experimental data are in good agreement with the Schlichting log law (Schlichting and Gersten, 2016) in the canonical boundary-layer.

To quantify the instantaneous wall-shear stress, intersecting laser beams of the LDV were focused directly above the location of the central MEMS sensor ($z^+ = 0$) where the wall-shear stress was quantified using the near-wall velocity gradient technique at $y^+ = yu_\tau/\nu = 4$, where $y = 0$ is the wall location. Three different MEMS sensors were used to measure the instantaneous wall-shear stress simultaneously across the span at each Reynolds number; see table 2. For each Reynolds number, MEMS sensors with appropriate size, sensitivity, and dynamic characteristics were utilised. The

(a)

(b)

(c)

Figure 3. (a) Displacement of the Moiré fringe pattern's sine curve on a MEMS sensor (MEMS 2) due to the applied wall-shear stress; (b) calibration curves of the MEMS wall-shear stress sensors. The inset demonstrates the calibration points in the lower end of the wall-shear stress spectrum for MEMS 5; (c) frequency response of a MEMS wall-shear stress sensor (MEMS 2). Thick black line represents the experimental results and the dashed blue line in derived from the analytical solution.

streamwise locations of the MEMS sensors were similar, whilst they were
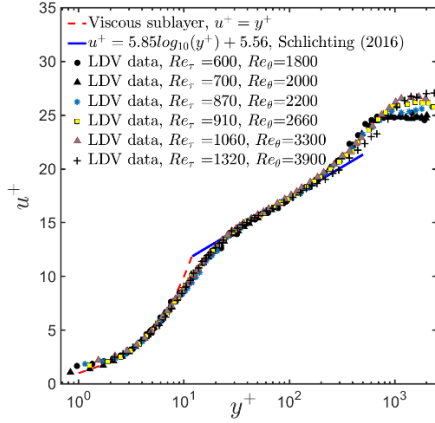
(a)

time signals of the instantaneous wall-shear stress captured simultaneously by the MEMS sensor and LDV is presented in
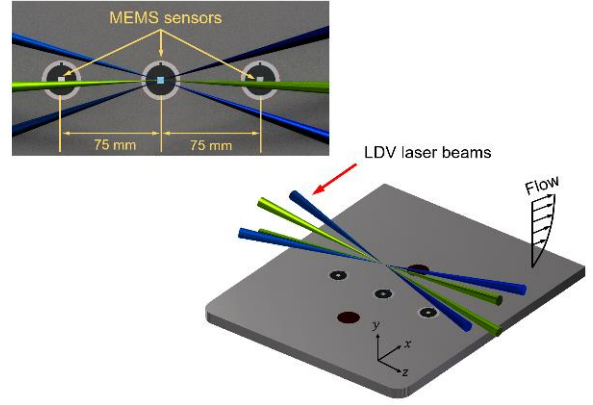
(b)
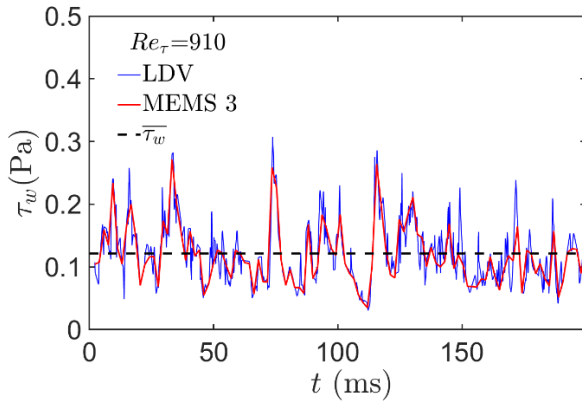
(c)
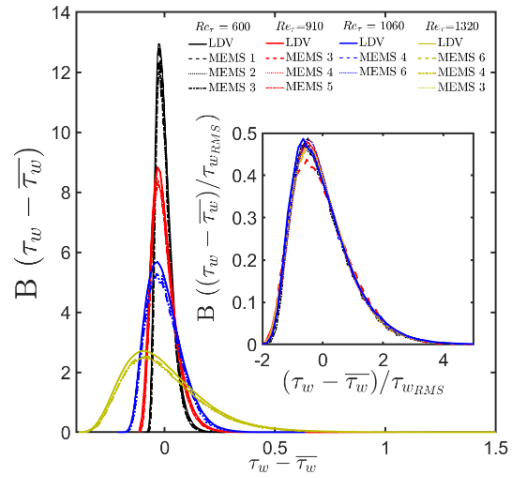
(d)

Figure 4. (a) Turbulent boundary-layer profile measured by LDV at $z^+ = 0$ for $Re_\tau = 600$ to 1320, (b) An illustration of MEMS and LDV configuration, (c) wall-shear stress time signals captured by a MEMS sensor and LDV, and (d) PDFs of fluctuating wall-shear stress measured by the MEMS sensors and LDV. Black lines represent the measurement at $Re_\tau = 600$, red lines represent the measurement at $Re_\tau = 910$, blue lines represent the measurement at $Re_\tau = 1060$, and orange lines represent the measurement at $Re_\tau = 1320$.

placed with a spatial pitch of 75 mm ($z^+ = \pm 1380$ to ± 2850) across the span, as shown in figure 4b. Up to 2×10^6 streamwise velocity data points were acquired with the LDV from within the viscous sub-layer for each Reynolds number. The statistical parameters of the instantaneous wall-shear stress such as the mean wall-shear stress, $\overline{\tau_w}$, standard deviation, SD_{τ_w}, skewness, S_{τ_w}, and kurtosis, K_{τ_w}, measured by the MEMS sensors and LDV were in very good agreement indicating that the MEMS sensors can accurately quantify the instantaneous wall-shear stress within the turbulent boundary-layer. To put this in context, as it is presented in table 2, at $Re_\tau = 1320$, the difference between the values of the mean wall-shear stress measured by the central MEMS sensor ($\overline{\tau_w} = 0.391$ Pa) and LDV ($\overline{\tau_w} = 0.399$ Pa) is $\approx 2\%$. This is within the uncertainty range of the measurement techniques as the accuracy of the MEMS sensors is quantified to be $1.4-2.4\%$ based on the calibration, and the accuracy of the LDV in the mean velocity measurements is $1-2\%$ (Whalley, et al. 2019). To investigate the performance of the MEMS sensors in capturing the wall-shear stress fluctuations, time signals of

instantaneous wall-shear stress captured simultaneously by the MEMS sensor and LDV is presented in figure 4c, where good agreement is observed in wall-shear stress time series.

Probability density functions (PDFs) of the fluctuating wall-shear stress, $B(\tau_w - \overline{\tau_w})$, acquired by the MEMS sensors and LDV are illustrated in figure 4d. Here, good agreement in the PDFs demonstrates that the MEMS sensors are accurately capturing the wall-shear stress fluctuations within the turbulent boundary-layer. It can be noticed that the distribution of the wall-shear stress data measured by all the devices are positively skewed. Moreover, the fluctuations in the wall-shear stress are super-Gaussian, which means there is a large probability of extreme fluctuations in the wall-shear stress. This agrees with the fluid flow physical behaviour near the wall region, where positive velocity fluctuations, and hence forward velocity gradients will be more likely to happen than backward velocity gradients (Gubian et al. 2019). Normalising the wall-shear stress data sets by $\tau_{w,RMS}$, collapses the data at $Re_\tau = 600$ to 1320. The positive tail on the normalised wall-shear stress fluctuations demonstrates that

the MEMS sensors can capture large events in the flow alongside with the LDV, where the values of $(\tau_w - \overline{\tau_w})/\tau_{w,RMS}$, extend beyond 7.5 for these devices. The normalised PDFs of the fluctuating wall-shear stress additionally indicates that no negative wall-shear stress values were detected by the MEMS sensors and LDV were captured. This is not unexpected as it was shown by Örlü and Schlatter (2011) that the contribution of the negative wall-shear stress values is less than 0.1% of the PDF.

Conclusion

Optical MEMS sensors have been developed to measure the instantaneous wall-shear stress within the turbulent boundary-layer. Sensor's characterisation results such as the sensitivity range of $23-730$ nm/Pa and the resonant frequency range of $1-8.4$ kHz, indicate that sensors can be developed for a range of applications. The performance of the MEMS wall-shear stress sensors has been investigated alongside LDV within turbulent boundary-layer flows, where the wall-shear stress data captured by these techniques were in excellent agreement, showing that the MEMS sensors can accurately detect the spatiotemporal wall-shear stress in turbulent boundary-layer flows.

Acknowledgments

REFERENCES

Alfredsson, P. H., and Johansson, A. V., 1988. "The fluctuating wall-shear stress and the velocity field in the viscous sublayer." *Physics of Fluids* 1026-1033.

Amidror, I., 2009. "The Theory of the Moiré Phenomenon: Volume I: Periodic Layers (Vol. 38). " *Springer Science & Business Media.*

Barlian, A.A., Park, S.J., Mukundan, V. and Pruitt, B.L., 2007. "Design and characterization of microfabricated piezoresistive floating element-based shear stress sensors. " *Sensors and Actuators A: Physical*, *134*(1), pp.77-87.

Barnard, C., Meloy, J., and Sheplak, M., 2016. "An instrumentation grade wall shear stress sensing system." *IEEE SENSORS.* IEEE. 1-3.

Chandrasekharan, V., Sells, J., Meloy, J., Arnold, D.P. and Sheplak, M., 2011. "A microscale differential capacitive direct wall-shear-stress sensor. " *Journal of microelectromechanical systems*, *20*(3), pp.622-635.

Chen, T.A., Mills, D., Chandrasekharan, V., Zmuda, H. and Sheplak, M., 2010, January. "Optical miniaturization of a MEMS-based floating element shear stress sensor with moiré amplification. " In *48th AIAA Aerospace Sciences Meeting Including the New Horizons Forum and Aerospace Exposition* (p. 498).

Diaz-Daniel, C., Laizet, S. and Vassilicos, J.C., 2017. "Wall shear stress fluctuations: Mixed scaling and their effects on velocity fluctuations in a turbulent boundary layer. " *Physics of Fluids*, *29*(5), p.055102.

Elsinga, G.E. and Westerweel, J., 2012. "Tomographic-PIV measurement of the flow around a zigzag boundary layer trip. " *Experiments in fluids*, *52*(4), pp.865-876.

Fraden, J., 2004. "*Handbook of modern sensors: physics, designs, and applications* (Vol. 3) ". New York: Springer.

Gubian, P.A., Stoker, J., Medvescek, J., Mydlarski, L. and Baliga, B.R., 2019. "Evolution of wall shear stress with Reynolds number in fully developed turbulent channel flow experiments. " *Physical Review Fluids*, *4*(7), p.074606.

Horowitz, S., Chen, T. A., Chandrasekaranm, V., Nishida, T., Cattafesta, L., Sheplak, M., and Tedjojuwono, K., 2004. "A micromachined geometric Moiré interferometric floating-element shear stress sensor." *42nd AIAA Aerospace Sciences Meeting and Exhibit'.* 1042.

Hutchins, N., and Choi, K., 2002. "Accurate measurements of local skin friction coefficient using hot-wire anemometry." *Progress in Aerospace Sciences* 421-446.

Li, Y., Chandrasekharan, V., Bertolucci, B., Nishida, T., Cattafesta, L., and Sheplak, M., 2008. "A MEMS shear stress sensor for turbulence measurements." *46th AIAA Aerospace Sciences Meeting and Exhibit'.* 269.

Mills, D. A., Patterson, W. C., Keane, C., and Sheplak, M., 2018. "Characterization of a fully-differential capacitive wall shear stress sensor for low-speed wind tunnels. " In *2018 AIAA Aerospace Sciences Meeting* (p. 0301).

Mills, D.A., Blood, D. and Sheplak, M., 2016. "Characterization of a sapphire optical wall shear stress sensor for high-temperature applications. " In *54th AIAA Aerospace Sciences Meeting* (p. 2016).

Örlü, R., and Vinuesa, R., 2020. "Instantaneous wall-shear-stress measurements: advances and application to near-wall extreme events." *Measurement Science and Technology* 112001.

Örlü, R. and Schlatter, P., 2011. "On the fluctuating wall-shear stress in zero pressure-gradient turbulent boundary layer flows. " *Physics of fluids*, *23*(2), p.021704.

Shajii, J., Ng, K.Y. and Schmidt, M.A., 1992. "A microfabricated floating-element shear stress sensor using wafer-bonding technology. " *Journal of Microelectromechanical Systems*, *1*(2), pp.89-94.

Schlichting, H. and Gersten, K., 2016. "Boundary-Layer Theory (pp. XXVIII–805). " *Verlag Berlin Heidelberg: Springer.*

Tseng, F.G. and Lin, C.J., 2003. "Polymer MEMS-based Fabry-Perot shear stress sensor. " *IEEE Sensors Journal*, *3*(6), pp.812-817.

Whalley, R. D., Dennis, D. J., Graham, M. D., and Poole, R. J., 2019. "An experimental investigation into spatiotemporal intermittencies in turbulent channel flow close to transition ." *Experiment in Fluids* 102.